Supplemental Material: Probing topological phase transitions via nonlinear Hall response in strained moiré dice lattice

Gourab Paul,[1] Srijata Lahiri,[1] Bilal Tanatar,[2] and Saurabh Basu[1]

[1] *Department of Physics, Indian Institute of Technology Guwahati, Guwahati-781039, Assam, India*
[2] *Department of Physics, Bilkent University, 06800 Bilkent, Ankara, Türkiye*

CONTENTS

SI. THE TIGHT-BINDING MODEL OF MONOLAYER DICE LATTICE

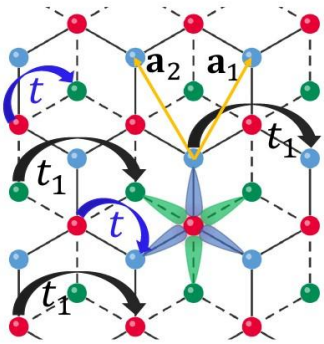

FIG. S1. Schematic diagram of the dice lattice. Blue, red, and green dots represent the A, B, and C sublattice atoms, respectively. The primitive lattice vectors are denoted by $\mathbf{a}_1$ and $\mathbf{a}_2$. The NN hopping amplitudes between $A \to B$ and $B \to C$ sites are labeled as t, while the NNN hopping amplitude among the $A \to A$, $B \to B$, and $C \to C$ sites is represented by t_1.

The Bravais lattice vectors of the dice lattice are given by $\mathbf{a}_1 = a\left(\frac{1}{2}, \frac{\sqrt{3}}{2}\right)$ and $\mathbf{a}_2 = a\left(-\frac{1}{2}, \frac{\sqrt{3}}{2}\right)$, where $a = \sqrt{3}d$ is the lattice constant and d is the nearest-neighbor (NN) bond length. We choose $d = 1.42$ Åas in the case for graphene. The NN hopping amplitude between the $A \to B$ and $B \to C$ sublattices is denoted by t, while the hopping amplitude for next-nearest-neighbor (NNN) interactions between the $A \to A$, $B \to B$, and $C \to C$ sublattices is denoted by t_1. The schematic representation of the dice lattice is shown in Fig. (S1). We take the B site as the origin. The relative position vectors of the three NN A sites with respect to the B site are given by: $\boldsymbol{\tau}_1^A = (0, d) = \frac{1}{3}(\mathbf{a}_1 + \mathbf{a}_2)$,

$\boldsymbol{\tau}_2^A = \left(-\frac{d\sqrt{3}}{2}, -\frac{d}{2}\right) = \boldsymbol{\tau}_1^A - \mathbf{a}_1$, and $\boldsymbol{\tau}_3^A = \left(\frac{d\sqrt{3}}{2}, -\frac{d}{2}\right) = \boldsymbol{\tau}_1^A - \mathbf{a}_2$. The three nearest-neighbor vectors from the B site to the C sites are simply the negative of those to the A sites: $\boldsymbol{\tau}_i^C = -\boldsymbol{\tau}_i^A$ for $i = 1, 2, 3$. The corresponding reciprocal lattice vectors are given by, $\mathbf{b}_1 = \frac{4\pi}{\sqrt{3}a}\left(\frac{\sqrt{3}}{2}, \frac{1}{2}\right)$ and $\mathbf{b}_2 = \frac{4\pi}{\sqrt{3}a}\left(-\frac{\sqrt{3}}{2}, \frac{1}{2}\right)$. The K_+ and K_- valleys are located at $\left(\frac{4\pi}{3a}, 0\right)$ and $\left(-\frac{4\pi}{3a}, 0\right)$, respectively.

In absence of NNN hopping t_1, the momentum-space Hamiltonian in the sublattice basis $(A_{\mathbf{k}} \quad B_{\mathbf{k}} \quad C_{\mathbf{k}})^T$ is given by [1]

$$H(\mathbf{k}) = \begin{pmatrix} 0 & f(\mathbf{k}) & 0 \\ f^*(\mathbf{k}) & 0 & \alpha f(\mathbf{k}) \\ 0 & \alpha f^*(\mathbf{k}) & 0 \end{pmatrix}, \tag{S1}$$

where the off-diagonal term is defined as, $f(\mathbf{k}) = -t(1+e^{-i\mathbf{k}.\mathbf{a}_1}+e^{-i\mathbf{k}.\mathbf{a}_2})$. Near the K valley, the low-energy expansion of $f(\mathbf{k})$ yields [2, 3]

$$f(q_x, q_y) = \frac{\sqrt{3}at}{2}(q_x - iq_y) = v_F(q_x - iq_y),$$

where $v_F = \frac{\sqrt{3}at}{2}$ is the Fermi velocity and $\mathbf{q}$ is measured relative to the K_+ point. Substituting this form into Eq. (S1), we obtain the effective low-energy Hamiltonian [4, 5]

$$H'(q_x, q_y) = v_F \begin{pmatrix} 0 & q_x - iq_y & 0 \\ q_x + iq_y & 0 & q_x - iq_y \\ 0 & q_x + iq_y & 0 \end{pmatrix}. \tag{S2}$$

Now including the NNN hopping amplitude t_1, the effective low-energy Hamiltonian near the K_+ valley can be written as

$$H(q_x, q_y) = v_F \begin{pmatrix} 0 & q_x - iq_y & 0 \\ q_x + iq_y & 0 & q_x - iq_y) \\ 0 & q_x + iq_y & 0 \end{pmatrix} + t_2 \begin{pmatrix} q^2 & 0 & 0 \\ 0 & q^2 & 0 \\ 0 & 0 & q^2 \end{pmatrix} \tag{S3}$$

where $t_2 = \frac{3}{4}t_1a^2 = \frac{\sqrt{3}at_1}{2t}v_F$ and $q^2 = q_x^2 + q_y^2$.

SII. THE INTERLAYER HAMILTONIAN OF UNSTRAINED TBDL

K_+ valley:
In the vicinity of K_+, the matrix elements of the interlayer Hamiltonian are given by [6–8]

$$U_{\tilde{X},X}(\mathbf{q}, \tilde{\mathbf{q}}) = \sum_{\mathbf{G},\tilde{\mathbf{G}}} w_{\tilde{X},X}(\mathbf{q} + \mathbf{K}_+ + \mathbf{G})\, e^{-i\mathbf{G}\cdot\boldsymbol{\tau}_X + i\tilde{\mathbf{G}}\cdot\boldsymbol{\tau}_{\tilde{X}}} \delta_{\mathbf{q}+\mathbf{K}_+ + \mathbf{G}, \tilde{\mathbf{q}}+\tilde{\mathbf{K}}_+ + \tilde{\mathbf{G}}}. \tag{S4}$$

Here, $\mathbf{G} = m_1\mathbf{b}_1 + m_2\mathbf{b}_2$ and $\tilde{\mathbf{G}} = m_1\tilde{\mathbf{b}}_1 + m_2\tilde{\mathbf{b}}_2$, where $\mathbf{b}_1$ ($\tilde{\mathbf{b}}_1$) and $\mathbf{b}_2$ ($\tilde{\mathbf{b}}_2$) are the reciprocal lattice vectors of layer-1 (layer-2), corresponding to its primitive lattice vectors $\mathbf{a}_1$ ($\tilde{\mathbf{a}}_1$) and $\mathbf{a}_2$ ($\tilde{\mathbf{a}}_2$). Now, we consider the A–B (Bernal) stacking configuration [7], under which the sublattice position vector of the atoms in both layers are given as, $\tau_A = \frac{1}{3}(\mathbf{a}_1 + \mathbf{a}_2)$, $\tau_B = 0$, $\tau_C = -\frac{1}{3}(\mathbf{a}_1 + \mathbf{a}_2)$, $\tau_{\tilde{A}} = \tau_0 + s\hat{e}_z - \frac{1}{3}(\tilde{\mathbf{a}}_1 + \tilde{\mathbf{a}}_2)$, $\tau_{\tilde{B}} = \tau_0 + s\hat{e}_z + \frac{1}{3}(\tilde{\mathbf{a}}_1 + \tilde{\mathbf{a}}_2)$, and $\tau_{\tilde{C}} = \tau_0 + s\hat{e}_z$. Here, s denotes the interlayer separation, and τ_0 is the relative in-plane translation vector of layer-2 with respect to layer-1. For simplicity, we consider $\tau_0 = 0$ in our analysis. Now replacing $\mathbf{G}$ and $\tilde{\mathbf{G}}$ in Eq. (S4), the interlayer Hamiltonian takes the form

$$U_{\tilde{X},X}(\mathbf{q}, \tilde{\mathbf{q}}) = \sum_{m_1,m_2} w_{\tilde{X},X}(\mathbf{q}+\mathbf{K}_+ + m_1\mathbf{b}_1 + m_2\mathbf{b}_2)\, e^{-i(m_1\mathbf{b}_1+m_2\mathbf{b}_2).\boldsymbol{\tau}_X + i(m_1\tilde{\mathbf{b}}_1+m_2\tilde{\mathbf{b}}_2).\boldsymbol{\tau}_{\tilde{X}}} \delta_{\mathbf{q}+\mathbf{K}_+ + m_1\mathbf{b}_1+m_2\mathbf{b}_2, \tilde{\mathbf{q}}+\tilde{\mathbf{K}}_+ + m_1\tilde{\mathbf{b}}_1+m_2\tilde{\mathbf{b}}_2}. \tag{S5}$$

The term $\delta_{\mathbf{q}+\mathbf{K}_+ + m_1\mathbf{b}_1+m_2\mathbf{b}_2, \tilde{\mathbf{q}}+\tilde{\mathbf{K}}_+ + m_1\tilde{\mathbf{b}}_1+m_2\tilde{\mathbf{b}}_2}$ in Eq. (S7) implies that interlayer scattering between layer-1 and layer-2 is only allowed for specific combinations of (m_1, m_2), for which the coupling $w_{X,\tilde{X}}(\mathbf{q} + \mathbf{K}_+ + m_1\mathbf{b}_1 + m_2\mathbf{b}_2)$ is maximized. The scattering matrices $U_{\mathbf{q}_b}$, $U_{\mathbf{q}_{tr}}$, and $U_{\mathbf{q}_{tl}}$ correspond to momentum transfers $\mathbf{q}_b$, $\mathbf{q}_{tr}$, and $\mathbf{q}_{tl}$,

arising from the combinations of $(m_1, m_2) = (0,0),\ (0,1),$ and $(-1,0)$, respectively. Now the interlayer Hamiltonian corresponding to K_+ valley is given by

$$\begin{aligned} U(\mathbf{q},\tilde{\mathbf{q}}) &= \begin{pmatrix} U_{\tilde{A},A} & U_{\tilde{B},A} & U_{\tilde{C},A} \\ U_{\tilde{A},B} & U_{\tilde{B},B} & U_{\tilde{C},B} \\ U_{\tilde{A},C} & U_{\tilde{B},C} & U_{\tilde{C},C} \end{pmatrix} \\ &= \begin{pmatrix} w_1 & w_2 & w_3 \\ w_2 & w_1 & w_2 \\ w_3 & w_2 & w_1 \end{pmatrix} \delta_{\mathbf{q}-\tilde{\mathbf{q}}-\mathbf{q}_b} + \begin{pmatrix} w_1 e^{i\phi} & w_2 & w_3 e^{-i\phi} \\ w_2 e^{-i\phi} & w_1 e^{i\phi} & w_2 \\ w_3 & w_2 e^{-i\phi} & w_1 e^{i\phi} \end{pmatrix} \delta_{\mathbf{q}-\tilde{\mathbf{q}}-\mathbf{q}_{tr}} + \begin{pmatrix} w_1 e^{-i\phi} & w_2 & w_3 e^{i\phi} \\ w_2 e^{i\phi} & w_1 e^{-i\phi} & w_2 \\ w_3 & w_2 e^{i\phi} & w_1 e^{-i\phi} \end{pmatrix} \delta_{\mathbf{q}-\tilde{\mathbf{q}}-\mathbf{q}_{tl}} \\ &= U_{\mathbf{q}_b}\delta_{\mathbf{q}-\tilde{\mathbf{q}}-\mathbf{q}_b} + U_{\mathbf{q}_{tr}}\delta_{\mathbf{q}-\tilde{\mathbf{q}}-\mathbf{q}_{tr}} + U_{\mathbf{q}_{tl}}\delta_{\mathbf{q}-\tilde{\mathbf{q}}-\mathbf{q}_{tl}} \end{aligned} \tag{S6}$$

The matrices $U_{\mathbf{q}_b},\ U_{\mathbf{q}_{tr}},\ U_{\mathbf{q}_{tl}}$, which describe the interlayer coupling at K_+ valley associated with each momentum transfer, take the following forms: $U_{\mathbf{q}_b} = \begin{pmatrix} w_1 & w_2 & w_3 \\ w_2 & w_1 & w_2 \\ w_3 & w_2 & w_1 \end{pmatrix}$, $U_{\mathbf{q}_{tr}} = \begin{pmatrix} w_1 e^{i\phi} & w_2 & w_3 e^{-i\phi} \\ w_2 e^{-i\phi} & w_1 e^{i\phi} & w_2 \\ w_3 & w_2 e^{-i\phi} & w_1 e^{i\phi} \end{pmatrix}$, $U_{\mathbf{q}_{tl}} = \begin{pmatrix} w_1 e^{-i\phi} & w_2 & w_3 e^{i\phi} \\ w_2 e^{i\phi} & w_1 e^{-i\phi} & w_2 \\ w_3 & w_2 e^{i\phi} & w_1 e^{-i\phi} \end{pmatrix}$ (with $\phi = 2\pi/3$).

K_- valley:
In the vicinity of K_-, the matrix elements of the interlayer Hamiltonian are given by [6–8]

$$U_{\tilde{X},X}(\mathbf{q},\tilde{\mathbf{q}}) = \sum_{m_1,m_2} w_{\tilde{X},X}(\mathbf{q}+\mathbf{K}_- + m_1\mathbf{b}_1 + m_2\mathbf{b}_2)\, e^{-i(m_1\mathbf{b}_1+m_2\mathbf{b}_2).\boldsymbol{\tau}_X + i(m_1\tilde{\mathbf{b}}_1+m_2\tilde{\mathbf{b}}_2).\boldsymbol{\tau}_{\tilde{X}}} \delta_{\mathbf{q}+\mathbf{K}_- + m_1\mathbf{b}_1+m_2\mathbf{b}_2, \tilde{\mathbf{q}}+\tilde{\mathbf{K}}_- + m_1\tilde{\mathbf{b}}_1+m_2\tilde{\mathbf{b}}_2}. \tag{S7}$$

The term $\delta_{\mathbf{q}+\mathbf{K}_- + m_1\mathbf{b}_1+m_2\mathbf{b}_2, \tilde{\mathbf{q}}+\tilde{\mathbf{K}}_- + m_1\tilde{\mathbf{b}}_1+m_2\tilde{\mathbf{b}}_2}$ in Eq. (S7) implies that interlayer scattering between layer-1 and layer-2 is only allowed for specific combinations of (m_1, m_2), for which the coupling $w_{X,\tilde{X}}(\mathbf{q} + \mathbf{K}_- + m_1\mathbf{b}_1 + m_2\mathbf{b}_2)$ is maximized. The scattering matrices $U_{-\mathbf{q}_b}$, $U_{-\mathbf{q}_{tr}}$, and $U_{-\mathbf{q}_{tl}}$ correspond to momentum transfers $\mathbf{q}_b$, $\mathbf{q}_{tr}$, and $\mathbf{q}_{tl}$, arising from the combinations of $(m_1, m_2) = (0,0),\ (0,-1),$ and $(1,0)$, respectively. Now the interlayer Hamiltonian corresponding to K_+ valley is given by

$$\begin{aligned} U(\mathbf{q},\tilde{\mathbf{q}}) &= \begin{pmatrix} U_{\tilde{A},A} & U_{\tilde{B},A} & U_{\tilde{C},A} \\ U_{\tilde{A},B} & U_{\tilde{B},B} & U_{\tilde{C},B} \\ U_{\tilde{A},C} & U_{\tilde{B},C} & U_{\tilde{C},C} \end{pmatrix} \\ &= \begin{pmatrix} w_1 & w_2 & w_3 \\ w_2 & w_1 & w_2 \\ w_3 & w_2 & w_1 \end{pmatrix} \delta_{\mathbf{q}-\tilde{\mathbf{q}}+\mathbf{q}_b} + \begin{pmatrix} w_1 e^{-i\phi} & w_2 & w_3 e^{i\phi} \\ w_2 e^{i\phi} & w_1 e^{-i\phi} & w_2 \\ w_3 & w_2 e^{i\phi} & w_1 e^{-i\phi} \end{pmatrix} \delta_{\mathbf{q}-\tilde{\mathbf{q}}+\mathbf{q}_{tr}} + \begin{pmatrix} w_1 e^{i\phi} & w_2 & w_3 e^{-i\phi} \\ w_2 e^{-i\phi} & w_1 e^{i\phi} & w_2 \\ w_3 & w_2 e^{-i\phi} & w_1 e^{i\phi} \end{pmatrix} \delta_{\mathbf{q}-\tilde{\mathbf{q}}+\mathbf{q}_{tl}} \\ &= U_{-\mathbf{q}_b}\delta_{\mathbf{q}-\tilde{\mathbf{q}}+\mathbf{q}_b} + U_{-\mathbf{q}_{tr}}\delta_{\mathbf{q}-\tilde{\mathbf{q}}+\mathbf{q}_{tr}} + U_{-\mathbf{q}_{tl}}\delta_{\mathbf{q}-\tilde{\mathbf{q}}+\mathbf{q}_{tl}} \end{aligned} \tag{S8}$$

The matrices $U_{-\mathbf{q}_b},\ U_{-\mathbf{q}_{tr}},\ U_{-\mathbf{q}_{tl}}$, which describe the interlayer coupling at K_- valley associated with each momentum transfer, take the following forms: $U_{-\mathbf{q}_b} = \begin{pmatrix} w_1 & w_2 & w_3 \\ w_2 & w_1 & w_2 \\ w_3 & w_2 & w_1 \end{pmatrix}$, $U_{-\mathbf{q}_{tr}} = \begin{pmatrix} w_1 e^{-i\phi} & w_2 & w_3 e^{i\phi} \\ w_2 e^{i\phi} & w_1 e^{-i\phi} & w_2 \\ w_3 & w_2 e^{i\phi} & w_1 e^{-i\phi} \end{pmatrix}$, $U_{-\mathbf{q}_{tl}} = \begin{pmatrix} w_1 e^{i\phi} & w_2 & w_3 e^{-i\phi} \\ w_2 e^{-i\phi} & w_1 e^{i\phi} & w_2 \\ w_3 & w_2 e^{-i\phi} & w_1 e^{i\phi} \end{pmatrix}$ (with $\phi = 2\pi/3$).

Now, taking both valleys into account, the general expression for the interlayer Hamiltonian associated with the

K_ζ valley can be written as

$$\begin{aligned} U_\zeta(\mathbf{q},\tilde{\mathbf{q}}) &= \begin{pmatrix} U_{\tilde{A},A} & U_{\tilde{B},A} & U_{\tilde{C},A} \\ U_{\tilde{A},B} & U_{\tilde{B},B} & U_{\tilde{C},B} \\ U_{\tilde{A},C} & U_{\tilde{B},C} & U_{\tilde{C},C} \end{pmatrix} \\ &= \begin{pmatrix} w_1 & w_2 & w_3 \\ w_2 & w_1 & w_2 \\ w_3 & w_2 & w_1 \end{pmatrix} \delta_{\mathbf{q}-\tilde{\mathbf{q}}-\zeta\mathbf{q}_b} + \begin{pmatrix} w_1 e^{i\zeta\phi} & w_2 & w_3 e^{-i\zeta\phi} \\ w_2 e^{-i\zeta\phi} & w_1 e^{i\zeta\phi} & w_2 \\ w_3 & w_2 e^{-i\zeta\phi} & w_1 e^{i\zeta\phi} \end{pmatrix} \delta_{\mathbf{q}-\tilde{\mathbf{q}}-\zeta\mathbf{q}_{tr}} + \begin{pmatrix} w_1 e^{-i\zeta\phi} & w_2 & w_3 e^{i\zeta\phi} \\ w_2 e^{i\zeta\phi} & w_1 e^{-i\zeta\phi} & w_2 \\ w_3 & w_2 e^{i\zeta\phi} & w_1 e^{-i\zeta\phi} \end{pmatrix} \delta_{\mathbf{q}-\tilde{\mathbf{q}}-\zeta\mathbf{q}_{tl}} \\ &= U_{\zeta\mathbf{q}_b}\delta_{\mathbf{q}-\tilde{\mathbf{q}}-\zeta\mathbf{q}_b} + U_{\zeta\mathbf{q}_{tr}}\delta_{\mathbf{q}-\tilde{\mathbf{q}}-\zeta\mathbf{q}_{tr}} + U_{\zeta\mathbf{q}_{tl}}\delta_{\mathbf{q}-\tilde{\mathbf{q}}-\zeta\mathbf{q}_{tl}} \end{aligned} \tag{S9}$$

SIII. THE INTRALAYER AND INTERLAYER HAMILTONIAN FOR STRAINED TBDL

Including both NN and NNN hoppings along with a staggered onsite mass term ΔS_3, the low energy intralayer Hamiltonian of the constituent monolayers of TBDL can be described in terms of massless Dirac fermions, where the top (bottom) layer of the TBDL is rotated by an angle $\theta/2$ ($-\theta/2$), as

$$H_{t/b,\zeta}(\theta/2) = v_F \mathcal{R}_{\mp\theta/2}\boldsymbol{q}.(\zeta S_1, S_2) + t_2 \mathcal{I}_3 q^2 + \Delta S_3, \tag{S10}$$

where $v_F = 6326.1$ meV·Å, $t_2 = \frac{\sqrt{3}at_1}{2t} v_F$, $\mathcal{I}_3 = \begin{pmatrix} 1 & 0 & 0 \\ 0 & 1 & 0 \\ 0 & 0 & 1 \end{pmatrix}$, and $\mathcal{R}_\theta$ denotes the rotational operator. The momentum $\mathbf{q} = \mathbf{k} - \mathbf{K}_\zeta$ is defined relative to the original Brillouin zone (BZ) corner $\mathbf{K}_\zeta$ of the monolayer dice lattice and S_i ($i = 1, 2, 3$) denotes the matrix representation of the spin-1 operators in the S_3 eigenbasis [9].

The effect of strain can be captured by the linear strain tensor $\mathcal{E}$, which maps an arbitrary coordinate $\mathbf{r}$ to a new coordinate given by

$$\mathbf{r}' = (\mathbb{I} + \mathcal{E})\,\mathbf{r}. \tag{S11}$$

Consequently, the corresponding transformation in momentum space is expressed as

$$\mathbf{q}' = (\mathbb{I} + \mathcal{E}^T)^{-1}\mathbf{q} \;\approx\; (\mathbb{I} - \mathcal{E}^T)\,\mathbf{q}, \tag{S12}$$

where the approximation is valid for linear order in the strain tensor. From this point onward, a prime on any quantity denotes that it is evaluated in the presence of strain.

For a uniaxial strain of magnitude $\mathcal{E}_p$ applied along a direction making an angle Φ with respect to the zigzag axis, the strain tensor takes the explicit form [10, 11]

$$\begin{aligned} \mathcal{E} &= R_\Phi \begin{pmatrix} \mathcal{E}_p & 0 \\ 0 & -\sigma\mathcal{E}_p \end{pmatrix} R_\Phi^{-1} \\ &= \mathcal{E}_p \begin{pmatrix} \cos^2\Phi - \sigma\sin^2\Phi & (1+\sigma)\cos\Phi\sin\Phi \\ (1+\sigma)\cos\Phi\sin\Phi & \sin^2\Phi - \sigma\cos^2\Phi \end{pmatrix}, \end{aligned} \tag{S13}$$

where $\sigma = 0.165$ is the Poisson ratio of the dice lattice, which is also taken to be the same as graphene [11]. The applied strain influences both the bottom layer Hamiltonian and the interlayer tunneling. In particular, for the bottom layer, strain generates an effective gauge field [10, 12] given by

$$\mathbf{A} = \frac{\beta}{d}\left(\mathcal{E}_{xx} - \mathcal{E}_{yy}\,, -2\mathcal{E}_{xy}\right), \tag{S14}$$

where $\beta = 1.57$ is the Grüneisen parameter [10], which is also taken to be the same as graphene. Upon performing the substitution $\mathbf{q} \to \mathbf{q} + \zeta\mathbf{A}$, the strained bottom-layer Hamiltonian can be written as

$$H'_{b,\zeta} = v_F\, R_{\theta/2}\left[(\mathbb{I} + \mathcal{E}^T)\,\mathbf{q}' + \zeta\mathbf{A}\right].(\zeta S_1, S_2) + \Delta S_3. \tag{S15}$$

The positions of the Dirac points in the bottom layer in the presence of this gauge field, are shifted to [10]

$$\mathcal{D}_\zeta = \left(\mathbb{I} - \mathcal{E}^T\right)\,\mathbf{K}_{b,\zeta} - \zeta\,\mathbf{A}. \tag{S16}$$

The interlayer tunneling is likewise affected by strain, as it modifies the momentum transfer between the layers. Because the momentum in the bottom layer is transformed, the corresponding transferred momenta become

$$\begin{aligned}
\zeta\mathbf{q}'_b &= R_{-\frac{\theta}{2}}(\mathbb{I}-\mathcal{E}^T)\mathbf{K}_\zeta - R_{\frac{\theta}{2}}\mathbf{K}_\zeta,\\
\zeta\mathbf{q}'_{tr} &= R_{-\frac{\theta}{2}}(\mathbb{I}-\mathcal{E}^T)(\mathbf{K}_\zeta+\zeta\mathbf{b}_2) - R_{\frac{\theta}{2}}(\mathbf{K}_\zeta+\zeta\mathbf{b}_2),\\
\zeta\mathbf{q}'_{tl} &= R_{-\frac{\theta}{2}}(\mathbb{I}-\mathcal{E}^T)(\mathbf{K}_\zeta-\zeta\mathbf{b}_1) - R_{\frac{\theta}{2}}(\mathbf{K}_\zeta-\zeta\mathbf{b}_1).
\end{aligned} \tag{S17}$$

Under these modifications, the strained interlayer Hamiltonian can be expressed as

$$U'_\zeta(\mathbf{q},\tilde{\mathbf{q}}) \;=\; U'_{\zeta\mathbf{q}'_b}\delta_{\mathbf{q}-\tilde{\mathbf{q}}-\zeta\mathbf{q}'_b} + U'_{\zeta\mathbf{q}'_{tr}}\delta_{\mathbf{q}-\tilde{\mathbf{q}}-\zeta\mathbf{q}'_{tr}} + U'_{\zeta\mathbf{q}'_{tl}}\delta_{\mathbf{q}-\tilde{\mathbf{q}}-\zeta\mathbf{q}'_{tl}}. \tag{S18}$$

The hopping matrices remain unchanged and preserve their original structure:

$$U'^{\tilde{\alpha}\beta}_{\zeta\mathbf{q}'_b} \;=\; w_{\tilde{\alpha}\beta} = U^{\tilde{\alpha}\beta}_{\zeta\mathbf{q}_b}, \tag{S19}$$

$$\begin{aligned}
U'^{\tilde{\alpha}\beta}_{\zeta\mathbf{q}'_{tr}} &= w_{\tilde{\alpha}\beta}e^{i\zeta\left(-\mathbf{b}_2\cdot\boldsymbol{\tau}_\beta+\tilde{\mathbf{b}}'_2\cdot\boldsymbol{\tau}'_{\tilde{\alpha}}\right)}\\
&= w_{\tilde{\alpha}\beta}e^{i\zeta\left(-\mathbf{b}_2\cdot\boldsymbol{\tau}_\beta+\tilde{\mathbf{b}}_2\cdot\boldsymbol{\tau}_{\tilde{\alpha}}\right)} = U^{\tilde{\alpha}\beta}_{\zeta\mathbf{q}_{tr}},
\end{aligned} \tag{S20}$$

$$\begin{aligned}
U'^{\tilde{\alpha}\beta}_{\zeta\mathbf{q}'_{tl}} &= w_{\tilde{\alpha}\beta}e^{i\zeta\left(\mathbf{b}_1\cdot\boldsymbol{\tau}_\beta-\tilde{\mathbf{b}}'_1\cdot\boldsymbol{\tau}'_{\tilde{\alpha}}\right)}\\
&= w_{\tilde{\alpha}\beta}e^{i\zeta\left(\mathbf{b}_1\cdot\boldsymbol{\tau}_\beta-\tilde{\mathbf{b}}_1\cdot\boldsymbol{\tau}_{\tilde{\alpha}}\right)} = U^{\tilde{\alpha}\beta}_{\zeta\mathbf{q}_{tl}}.
\end{aligned} \tag{S21}$$

Here, $\alpha,\beta = A,B$, and C denote the sublattice indices, with $w_{\tilde{A}A} = w_{\tilde{B}B} = w_{\tilde{C}C} = w_1$, $w_{\tilde{A}B} = w_{\tilde{B}A} = w_{\tilde{B}C} = w_{\tilde{C}A} = w_2$, and $w_{\tilde{A}C} = w_{\tilde{C}A} = w_3$. In obtaining these results, we used $\tilde{\mathbf{b}}'_{1,2}\cdot\boldsymbol{\tau}'_{\tilde{\alpha}} = \tilde{\mathbf{b}}_{1,2}\cdot\boldsymbol{\tau}_{\tilde{\alpha}}$, and neglected any strain dependence of the tunneling amplitudes.

SIV. BAND STRUCTURE OF STRAINED TBDL

In this section, we show the band structures of TBDL at the magic angle $\theta = 1.08^\circ$ in the presence of different strain values are plotted along the high-symmetry path $\mathrm{K_t} \to \mathrm{K_b} \to \Gamma \to \mathrm{K_t}$, where the lowest band at the middle band edge is highlighted in red color. Panel (a) representing the energy dispersions in the chiral limit of the system, implemented by setting $w_1 = w_3 = 0$ and $w_2 = 110.7$ meV, while panel (b) corresponds to the the broken chiral limit of the system, obtained by setting $w_1 = w_3 = 60$ meV and $w_2 = 110.7$ meV. The calculations for both the panels are carried out using the Fermi velocity $v_F = 6326.1$ meV·Å and $t_2 = 0.001\,v_F$, with $\Delta = 170$ meV for panels (a) and $\Delta = 60$ meV for panel (b). The energy dispersions are shown for the three distinct increasing strain values, $\mathcal{E}_p = 0.2\%$, 0.4%, and 0.6%, represented by solid, dashed and, dotted lines, respectively.

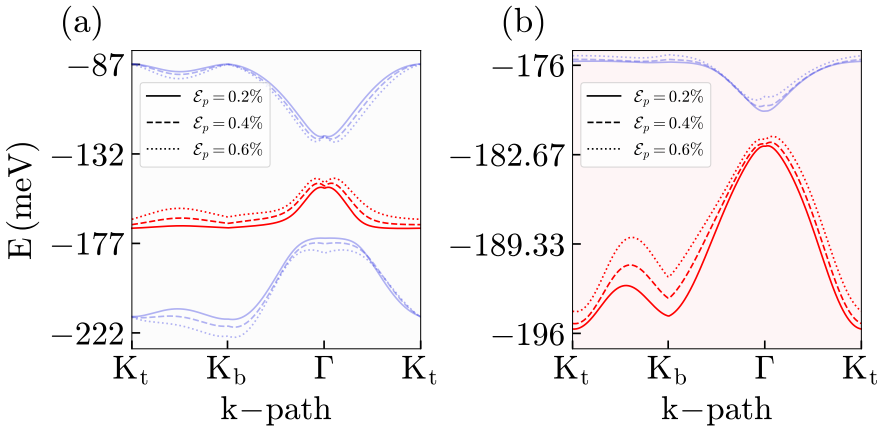

FIG. S2. Band structures of TBDL at the magic angle $\theta = 1.08^\circ$ in the presence of different strain values.

SV. BERRY CURVATURE AND BERRY CURVATURE DIPOLE DISTRIBUTION

The distribution of the Berry curvature (Ω_z) and the BCD density ($\partial_{q_b}\Omega_z$ with $b = x, y$) in the K_+ valley, both in the presence and absence of $\mathcal{C}_3$ symmetry, are presented in Figs. S3[(a)–(c)] for the lowest band at the middle band edge (corresponding to the band index $n = 162$). Fig. S3(a) and Fig. S3(b) correspond to the chiral limit of the system ($w_1 = w_3 = 0$ and $w_2 = 110.7$ meV), with panel (a) representing the case with preserved $\mathcal{C}_3$ symmetry and panel (b) depicting the case with broken $\mathcal{C}_3$ symmetry. While Fig. S3(c), on the other hand, corresponds to the broken chiral symmetry regime ($w_1 = w_3 = 60$ meV and $w_2 = 110.7$ meV), where $\mathcal{C}_3$ symmetry of the system remains broken. We emphasize that the presence of TRS in TBDL, the Berry curvature satisfies $\Omega_{z,K_+}(\mathbf{q}) = -\Omega_{z,K_-}(-\mathbf{q})$. In presence of $\mathcal{C}_3$ symmetry (i.e., in the absence of strain), the Berry curvature and the BCD density shows symmetric patterns in the MBZ [see Fig. S3(a)]. Interestingly, we find that, in the presence of $\mathcal{C}_3$ symmetry, although each valley in TBDL exhibits large Berry curvature, but the total BCD (BCD density integrated over the whole BZ) vanishes identically. However, in any realistic systems strain can be applied to break the $\mathcal{C}_3$ symmetry, which in turn gives rise to a finite BCD in the system. In the presence of strain the BCD density shows asymmetric distributions [see Fig. S3(b) and Fig. S3(c)], which generate a net dipole within the moiré unit cell.

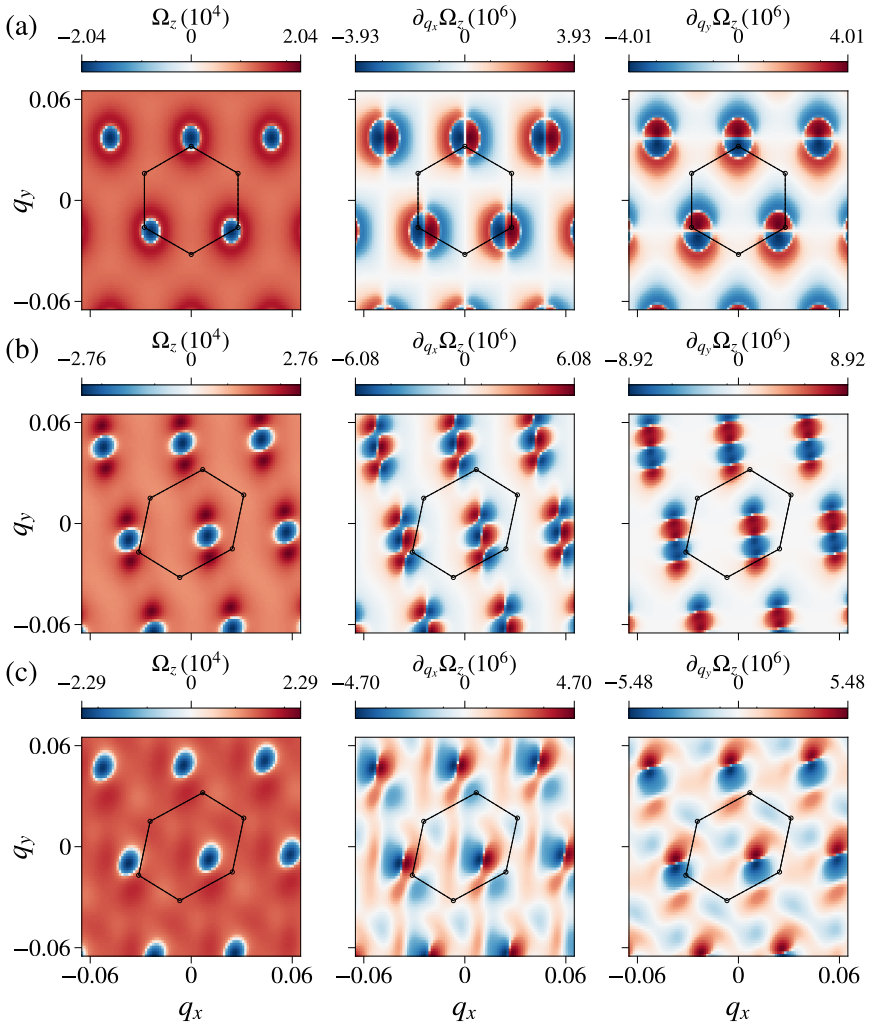

FIG. S3. The distribution of the Berry curvature Ω_z and the BCD density $\partial_{q_a}\Omega_z$ ($a = x, y$) for the lowest band at the middle band edge, plotted in the logarithmic scale, is shown in panels (a)-(c) for three distinct cases. Panel (a) represents the unstrained configuration of the system with preserved $\mathcal{C}_3$ symmetry in the chiral limit ($w_1 = w_3 = 0$ and $w_2 = 110.7$ meV), whereas panels (b) and (c) correspond to the broken $\mathcal{C}_3$ symmetry due to the presence of a strain $\mathcal{E}_p = 0.4\%$, with panel (b) corresponding to the chiral limit and panel (c) representing the broken chiral symmetry regime ($w_1 = w_3 = 60$ meV and $w_2 = 110.7$ meV) of the system. The calculations for all the panels are carried out using the Fermi velocity $v_F = 6326.1$ meV·Å and $t_2 = 0.001\,v_F$, with $\Delta = 170$ meV for panels (a) and (b), and $\Delta = 60$ meV for panel (c). Momenta are measured in units of Å^{-1}, Berry curvature in units of Å^2, while the dipole density in units of Å^3.

SVI. CHERN PHASE DIAGRAM OF THE BAND AT THE LOWER EDGE OF THE MIDDLE SUBBAND IN UNSTRAINED TBDL

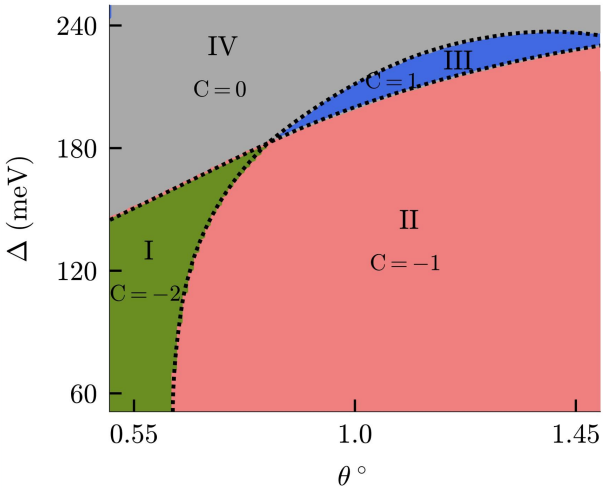

FIG. S4. Chern number phase diagram for the band index $n = 162$. The figure shows emergent topological phases for the lowest eigenstate of the middle sub-band of unstrained TBDL, as a function of the onsite mass Δ and the twist angle θ.

In this section, we analyze the topological phases that emerge corresponding to the K_+ valley in unstrained TBDL as a function of the onsite potential Δ and the twist angle θ. The phase diagram depicting the Chern number of the eigenstate with eigenvalue at the lower edge of the middle sub-band (band index $n = 162$), in the $\Delta - \theta$ plane and within the chiral symmetry regime, implemented by setting $w_1 = w_3 = 0$ and $w_2 = 110.7$ meV, is shown in Fig. S4. The emergence of multiple topological phases corresponding to Chern number $C = 1, -1$ and -2 is observed, separated by distinct transition lines. We observe that for high values of Δ, the band transitions into a completely trivial phase while for its lower values, the $C = -1$ phase is predominant.

SVII. PROBING DISTINCT TOPOLOGICAL PHASE TRANSITIONS MARKED BY CHERN NUMBER CHANGES $C = -2 \to C = -1$ AND $C = -2 \to C = 0$

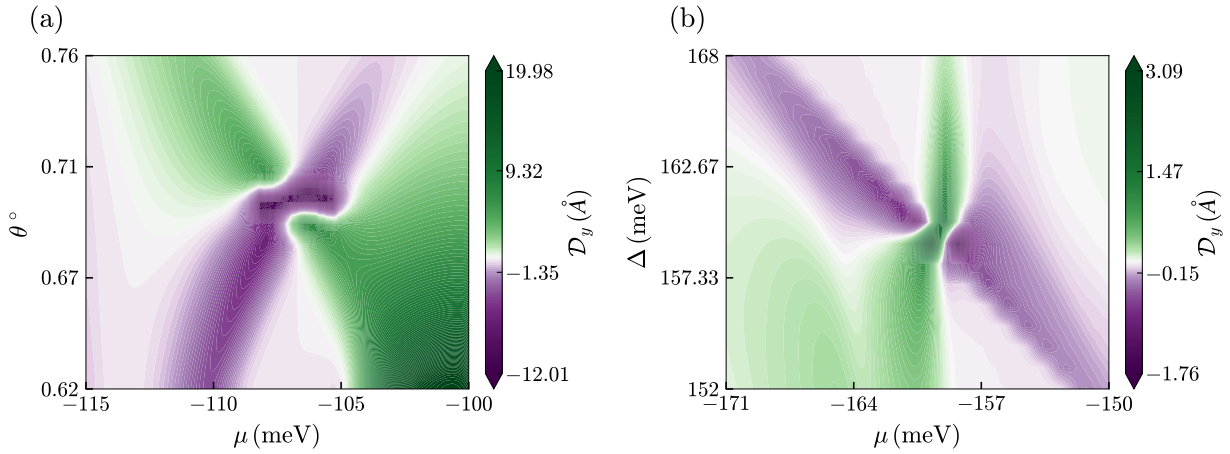

FIG. S5. Topological phase transitions identified through the variation of BCD in (a) the θ–μ plane, with Δ fixed at 120 meV, corresponding to the transition from Phase (I) to Phase (II), and (b) the Δ–μ plane, with θ fixed at 0.6°, corresponding to the transition from Phase (I) to Phase (IV).

In this section, we present the phase diagram of the BCD component $\mathcal{D}_y$ in the θ–μ plane for a fixed $\Delta = 120$ meV, as illustrated in Fig. S5(a), and in the Δ–μ plane, shown in Fig. S5(b), while keeping the twist angle fixed at $\theta = 0.6°$.

Fig. S5(a) corresponds to the topological phase transition from Phase (I) to Phase (II), whereas Fig. S5(b) represents the transition from Phase (I) to Phase (IV). The butterfly like structures in the colormap of $\mathcal{D}_y$ indicate points of phase transition which can be correlated directly with the Chern phase plot in Fig. 3 of the main manuscript. The lower two lobes of each butterfly pattern along a horizontal line (with θ fixed in Fig. S5(a) and Δ fixed in Fig. S5(b)) represent the values of $\mathcal{D}_y$ for the corresponding band at a given chemical potential μ. On the other hand, the sign reversal of $\mathcal{D}_y$ along a vertical line (with fixed μ) reflects the change in the sign of the BCD for the same band as a function of either θ or Δ, respectively. As evident from Fig. S5(a) and Fig. S5(b), the phase transitions occur near $\theta = 0.698°$ and $\Delta = 159.3$ meV, respectively. These results highlight the experimental significance of the BCD as an effective probe for identifying topological phase transitions.

SVIII. INFLUENCE OF TEMPERATURE ON THE BCD IN THE CHIRAL LIMIT

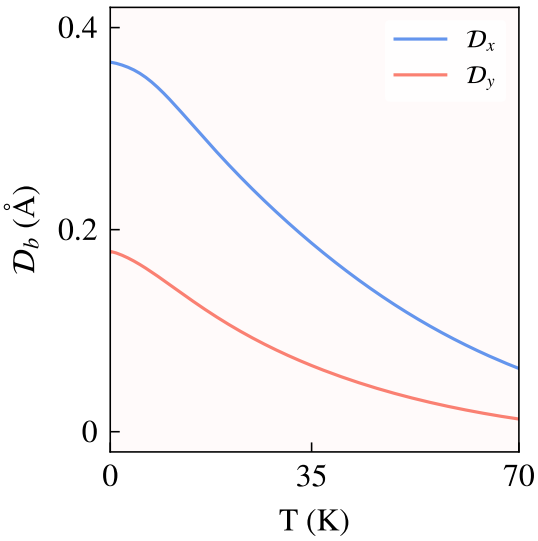

FIG. S6. Temperature dependence of the BCD components at the magic angle $\theta = 1.08°$ in the chiral limit of the system, implemented by setting $w_1 = w_3 = 0$ and $w_2 = 110.7$ meV, with $\Delta = 170$ meV at a strain $\mathcal{E}_p = 0.4\%$. The chemical potential is fixed at $\mu = -165.9$ meV.

So far, all the results we discussed have been obtained at a fixed temperature of $T = 4$ K. Now in-order to see the temperature dependence of BCD in TBDL, in this section we plot the BCD components, $\mathcal{D}_x$ and $\mathcal{D}_y$, as a function of temperature in the chiral limit of the system at the magic angle $\theta = 1.08°$, as shown in Fig. S6. Here, we fix the chemical potential at $\mu = -165.9$ meV. It is evident from the Fig. S6 that, as the temperature increases the dipole components gradually decreases. This can be attributed to the thermal broadening of the Fermi Dirac distribution function, thereby the reduction in its slope suppresses the magnitude of the dipole components. This behavior indicates that one could detect a strong NLH response at the low temperatures in TBDL. This temperature dependence of the BCD components in TBDL exhibits similar kind of behavior to that reported in the previous experimental studies on TBG [13] and twisted bilayer WTe_2 [14].

[1] E. Illes, *Properties of the α-T_3 Model*, Phd thesis, University of Guelph (2017).
[2] A. Raoux, M. Morigi, J.-N. Fuchs, F. Piéchon, and G. Montambaux, From dia- to paramagnetic orbital susceptibility of massless fermions, Phys. Rev. Lett. **112**, 026402 (2014).
[3] E. Illes, J. P. Carbotte, and E. J. Nicol, Hall quantization and optical conductivity evolution with variable berry phase in the $\alpha-T_3$ model, Phys. Rev. B **92**, 245410 (2015).
[4] M. Islam, K. Bhattacharyya, and S. Basu, Electron-phonon coupling induced topological phase transition in an $\alpha-T_3$ haldane-holstein model, Phys. Rev. B **110**, 045426 (2024).
[5] M. Islam and S. Basu, Conductance properties of $\alpha-T_3$ corbino disks, J. Phys.: Condens. Matter **37**, 205302 (2025).
[6] M. Koshino, Interlayer interaction in general incommensurate atomic layers, New Journal of Physics **17**, 015014 (2015).

[7] D. Ma, Y. G. Chen, Y. Yu, and X. Luo, Moiré semiconductors on the twisted bilayer dice lattice, Phys. Rev. B **109**, 155159 (2024).
[8] G. Paul, S. Lahiri, K. Bhattacharyya, and S. Basu, Emergent topology of flat bands in a twisted bilayer $\alpha-T_3$ lattice, Phys. Rev. B **113**, 035145 (2026).
[9] H. Georgi, *Lie Algebras in Particle Physics: From Isospin to Unified Theories*, 2nd ed., Frontiers in Physics, Vol. 54 (Perseus Books, Reading, MA, 1999).
[10] Z. Bi, N. F. Q. Yuan, and L. Fu, Designing flat bands by strain, Phys. Rev. B **100**, 035448 (2019).
[11] V. M. Pereira, A. H. Castro Neto, and N. M. R. Peres, Tight-binding approach to uniaxial strain in graphene, Phys. Rev. B **80**, 045401 (2009).
[12] J. Sun, T. Liu, Y. Du, and H. Guo, Strain-induced pseudo magnetic field in the $\alpha - T_3$ lattice, Phys. Rev. B **106**, 155417 (2022).
[13] J. Duan, Y. Jian, Y. Gao, H. Peng, J. Zhong, Q. Feng, J. Mao, and Y. Yao, Giant second-order nonlinear hall effect in twisted bilayer graphene, Phys. Rev. Lett. **129**, 186801 (2022).
[14] Z.-Y. Cao, A.-Q. Wang, X.-Y. Liu, T.-Y. Zhao, D. Yu, and Z.-M. Liao, Nonlinear hall effect and scaling law analysis in twisted bilayer WSe_2, Phys. Rev. B **111**, 125407 (2025).